



# Drivers of membrane fouling in the vanadium acetylacetonate flow battery

Rohit Rungta<sup>a</sup>, Kirk P. Smith<sup>a,b</sup>, Charles W. Monroe<sup>a,b,\*</sup>

<sup>a</sup> Department of Engineering Science, University of Oxford, Oxford, OX1 3PJ, United Kingdom

<sup>b</sup> The Faraday Institution, Harwell Campus, Didcot, OX11 0RA, United Kingdom

## ARTICLE INFO

### Keywords:

Redox flow battery  
Nonaqueous  
Membrane fouling  
Performance fade  
Crossover  
Electrolyzer

## ABSTRACT

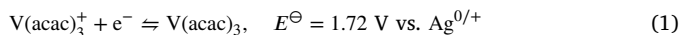
Vanadium acetylacetonate (V(acac)<sub>3</sub>) disproportionation electrochemistry promises a crossover-tolerant, high-voltage flow battery, but exhibits low efficiency and short cycle life. We show that membrane fouling, rather than a parasitic side reaction, dominates early performance fade. Crossover rates through porous membranes were estimated from voltage transients with an adaptive observer while cycling flow-through reactors. For 0.1 M V(acac)<sub>3</sub> and 0.3 M TEABF<sub>4</sub> in acetonitrile flowed countercurrently at 5.0 cm s<sup>-1</sup> parallel to the separator, fresh Daramic 175 and Celgard 4650 afforded active-species mass-transfer coefficients of 3.8 μm s<sup>-1</sup> and 7.5 μm s<sup>-1</sup>, respectively, which decreased and became non-Fickian as cycling progressed. At ±10 mA cm<sup>-2</sup> from 0%–20% state of charge, voltage efficiency with Celgard fell from 96% to 60% over 27 cycles. Separator replacement restored the coulombic and voltage efficiencies, which repeated their first progression. Impedance spectra from series-connected canary cells reveal that separator resistances remain stable during open-circuit exposure to charged single electrolytes, but increase under applied current or open-circuit contact with differently charged electrolytes.

## 1. Introduction

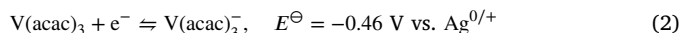
As readily accessible oil and gas reserves deplete and global climate change becomes more broadly disquieting, the adoption of renewable energy sources has accelerated (Palmer, 2019; Carley et al., 2018). To cope with the essential irregularity of renewable energy production from sunlight and wind, policymakers are looking to energy storage options (Luo et al., 2021; Judson and Pike, 2015). Electrochemical storage stands out for its long operational lifetime and ability to hold energy for hours or days with minimal losses (Weber et al., 2011). Redox flow battery (RFB) systems additionally provide flexible charge capacity that can be rescaled independently of power capability.

Darling et al. identified low energy density, which raises both capital and operational costs per unit of energy stored, as a chief barrier to wide-scale RFB commercialization (Darling et al., 2014). The two main routes to increase RFB energy density are to formulate electrolytes that permit higher active-species concentrations or to develop reaction chemistries that support high cell potential (>2 V). Aqueous RFB electrolytes are constrained within the voltage window permitted by H<sub>2</sub> and O<sub>2</sub> evolution, but non-aqueous electrolytes can support higher cell voltages.

Below we consider the non-aqueous vanadium acetylacetonate (V(acac)<sub>3</sub>) RFB chemistry, first proposed by Liu et al. (2009). The V(acac)<sub>3</sub> RFB relies on two elementary half-reactions,

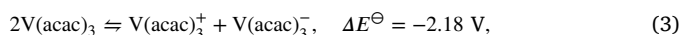


at the positive electrode and



at the negative electrode (Shinkle et al., 2012). Because the V(acac)<sub>3</sub> coordination complex undergoes outer-sphere electron transfers when oxidized or reduced, its reaction kinetics is fast at both electrodes (Shinkle et al., 2011), allowing discharge voltages near 2 V to be attained by flow cells operated at reasonable current densities (Saraidaridis and Monroe, 2019).

One-electron electrochemical disproportionation,



is the cell reaction when charging a V(acac)<sub>3</sub> RFB. Overall reactions of this type enable configurations in which the positive electrolyte and negative electrolyte are identical in their fully discharged states. In such ‘common-electrolyte’ systems, electrolyte mixing is reversible. This provides an inherent advantage over standard RFB chemistries because active-species crossover through the flow reactor’s separator membrane results in self-discharge, rather than driving irreversible composition change that necessitates periodic electrolyte regeneration. The crossover tolerance of common-electrolyte systems allows simple porous separators to be used instead of the costly ion-exchange membranes typically assumed essential for RFBs.

\* Corresponding author at: Department of Engineering Science, University of Oxford, Oxford, OX1 3PJ, United Kingdom.

E-mail address: [charles.monroe@eng.ox.ac.uk](mailto:charles.monroe@eng.ox.ac.uk) (C.W. Monroe).

This letter reports performance metrics including utilization, coulombic, voltage, and energy efficiencies, gathered from cycling RFB flow reactors that quantify  $V(\text{acac})_3$  crossover through porous separators. The measurements are intended to shed light on the trade-off between the lower capital costs unlocked by cheaper membranes and the higher operational losses incurred by crossover-related charge inefficiency. They also help to disentangle sources of performance degradation, pinpointing how changes in the separator cause performance metrics to vary as the RFB cycles.

Intermittent measurements of crossover rates and impedance spectra while cycling the  $V(\text{acac})_3$  RFB reactor system reveal that the vast majority of performance loss owes to fouling of the separator membrane, rather than the side reactions involving electrolyte components or environmental contaminants imputed by prior researchers (Escalante-García et al., 2015; Clegg and Hill, 2020). Although membrane fouling has been observed in several RFB chemistries before (Lehmann et al., 2022), the phenomenon has yet to be explained.

Additional experiments using secondary flow reactors connected in series with the main reactor – so-called ‘canary cells’ – were performed to clarify how operating conditions and differing electrolyte states drive separator degradation during long-term cycling. Key performance metrics and trends are discussed, with the aim of decoupling the signature of membrane fouling from those of self-discharge and electrolyte degradation. Independent understanding of these phenomena is critical when using flow reactors to evaluate the performance of a disproportionation RFB chemistry.

## 2. Experimental

Unless otherwise stated, all chemicals and materials were used as received. Cycling experiments and electrolyte handling were always conducted in an argon-filled (99.998%, BOC, UK) Inert Pure LabHE glovebox with atmospheric water and oxygen contents below 0.5 ppm.

### 2.1. Electrolyte preparation

Molecular sieves (4 Å, Fisher Scientific, UK) were dried at 250 °C for 24 h under vacuum and transferred to the glovebox while warm before use. HPLC-grade acetonitrile (Thermo Fisher, 99.9%, UK) was degassed with argon and purified with a PureSolv-Micro solvent purification system (Inert, UK). Purified acetonitrile (ACN) was transferred to the glovebox and further dried over the molecular sieves. After drying for 48 h, a C30 Karl Fischer Coulometric Titrator (Mettler-Toledo, UK) was used to confirm water content below 0.5 ppm.  $V(\text{acac})_3$  (98%, Strem, UK) was recrystallized with the anhydrous ACN and washed with anhydrous diethyl ether (Honeywell, 99.5%, UK) in the glovebox. The purified  $V(\text{acac})_3$  crystals were dried and stored in the glovebox. Tetraethylammonium tetrafluoroborate ( $\text{TEABF}_4$ , 99%, Sigma, UK) was stored in the glovebox and used as received.

### 2.2. Reactor design

The flow-through reactor designed by Smith and Monroe (2021), with a separator area of 2.20 cm<sup>2</sup> parallel to the flow direction and a compressed depth of 1.6 mm normal to the flow, was used for all cycling experiments; Fig. S1 of the supplementary information (SI) gives further details. Flow reactors were assembled and cycled in the glovebox. The electrodes were 3.18 mm thick carbon felt (Alfa-Aesar, UK), dried under vacuum at 250 °C for 48 h before reactor assembly. Separators – either Daramic 175 or Celgard 4560 – were rinsed in anhydrous ACN before use. Expanded polytetrafluoroethylene (ePTFE, Gore, USA) gaskets were used between the resin-impregnated graphite plate (Graphite-Store, USA) and separator. The four screws clamping the reactor assembly together were tightened to a torque of 40 in.lb. After this compression the reactor had a thickness of 1.6 mm

and a half-cell volume of 0.35 cm<sup>3</sup>. Chemically compatible diaphragm pumps (model FF-12, 1/428 fittings, DCB-4 wire control, FS 60X PEEK prefilter, KNF Neuberger, UK) were used for all experiments. Flow rates of 10 mL min<sup>-1</sup>, 26 mL min<sup>-1</sup>, and 51 mL min<sup>-1</sup> were employed, corresponding respectively to linear flowrates past the separator of 1.0 cm s<sup>-1</sup>, 2.5 cm s<sup>-1</sup>, and 5.0 cm s<sup>-1</sup>, as explained in the SI.

### 2.3. Cycling procedure

An Autolab PGSTAT 302N potentiostat (Metrohm, UK) was used to cycle the  $V(\text{acac})_3$  RFB. For charge/discharge tests, cells were charged up to 20% of the theoretical maximum state of charge (SOC), as computed via coulomb counting, at 10 mA cm<sup>-2</sup> (22 mA). Voltage cutoffs of 3.0 V for charging steps and 1.3 V for discharging steps were applied. Cells were held at open circuit (a 0 A applied current) for 15 s between charging and discharging steps to monitor the open-circuit potential as it relaxed.

Impedance measurements were conducted using an FRA32 module on the potentiostat. Impedance spectra were gathered every 10 cycles at 0% SOC (as established by an open-circuit hold after the cell discharged to 1.3 V), unless stated otherwise. The signal amplitude was set to 10 mV and frequencies ranged from 0.1 Hz to 100 kHz with 5 points per decade. Measuring an impedance spectrum typically took two minutes.

Every self-discharge experiment was run with a similar protocol, built up from three different cycling procedures: a regular cycle, an impedance cycle, and a self-discharge cycle. In a regular cycle, the cell was charged up to 30% of its theoretical maximum SOC by coulomb counting at 20 mA cm<sup>-2</sup> (44 mA), held at 0 A for 15 s, and subsequently discharged at 20 mA cm<sup>-2</sup> down to 1.3 V. The impedance cycle was identical to the regular cycle, aside from a two-minute impedance measurement being taken immediately before discharging according to the protocol described above. In self-discharge cycles, the cell was charged up to 100% of its theoretical maximum SOC by coulomb counting, after which it was held at 0 A until the voltage dropped below 2 V. In all self-discharge experiments, a regular cycle was run first as a ‘burn-in’ step, followed by an impedance cycle. Then, a 10-cycle loop consisting of one self-discharge cycle, an impedance cycle, and eight regular cycles was initiated. The 10-cycle loop was continued until the cell was unable to self-discharge fully, as indicated by a lack of an appreciable voltage change over an hour.

### 2.4. Experimental data

For clarity, all of the charge/discharge cycling profiles and impedance spectra gathered are not presented below. Results from every charge/discharge experiment and impedance measurement are available in a data repository that accompanies this article (Rungta, 2023). The repository also includes modified Matlab code for the adaptive observer along with outputs from the adaptive observer for all six self-discharge experiments.

The performance metrics reported include utilization efficiency (UE), coulombic efficiency (CE), voltage efficiency (VE), and energy efficiency (EE). These in turn are based on measurements of actual discharge capacity, actual charge capacity, and theoretical maximum capacity. Actual discharge capacity is defined as the cumulative charge passed during a discharge step before reaching the lower voltage cutoff; actual charge capacity is the cumulative charge passed during a charge step before reaching the specified charge input or the upper voltage cutoff, whichever comes first. The theoretical maximum capacity was determined by using the active-species molarities in the positive and negative electrolytes to calculate the maximum amount of charge that could be input, assuming the maximal active-species conversion allowed by the overall cell reaction and that as-prepared electrolytic solutions exist in a fully discharged state. UE is the ratio of actual discharge capacity to theoretical maximum capacity. CE is the ratio of actual discharge capacity to actual charge capacity, and provides

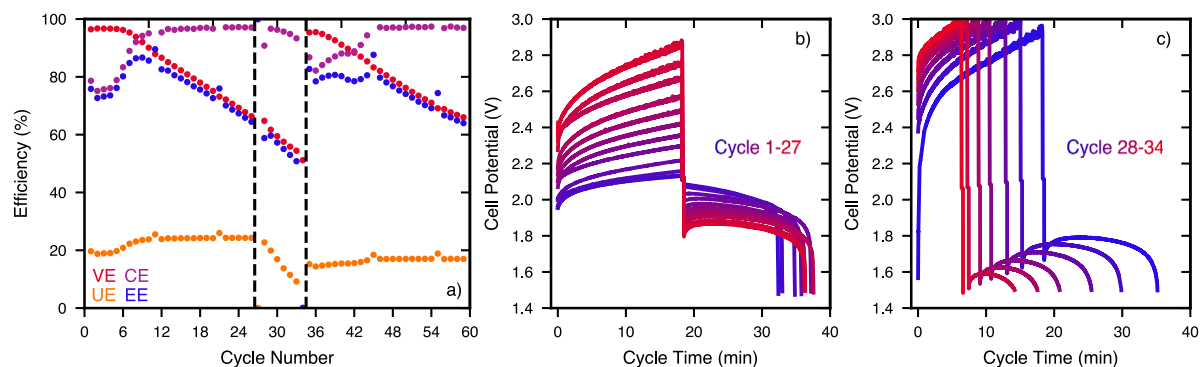


**Fig. 1.** (a) Voltage (VE), coulombic (CE), utilization (UE), and energy (EE) efficiencies and (b, c) galvanostatic charge/discharge data for the first 35 cycles for the 0.1 M V(acac)<sub>3</sub>, 0.3 M TEABF<sub>4</sub> RFB in a countercurrent and zero-gap flow configuration with a microporous Celgard 4560 separator. The cell was cycled to a theoretical SOC of 20% via coulomb counting at 10 mA cm<sup>-2</sup>. The identities of the positive and negative reservoirs were switched by discharging twice before cycle 28. After cycle 34, the separator was replaced.

a useful metric for assessing the charge reversibility of each cycle. CE losses are most often attributed to self-discharge (active-species crossover) or electrolyte degradation (irreversible side reactions). VE is the ratio of the time-averaged voltage measured during a discharge step to the time-averaged voltage measured during the prior charge step; it gives insight into ohmic, kinetic, and other dynamical losses. EE is the ratio of the energy output during a discharge step – determined by integrating current times instantaneous voltage over the duration of the step – to the energy input during the prior charge step, calculated in a similar way. Because the experiments were run with constant currents of equal magnitude during charge and discharge steps, the EE values reported here simply combine information from both CE and VE:  $EE = VE \times CE$ .

### 3. Results and discussion

#### 3.1. Cell performance

Saraïdaridis reported stable cycling of V(acac)<sub>3</sub> for 160 cycles (Saraïdaridis and Monroe, 2019) and postulated that reservoir imbalance caused the cell's eventual failure. After adding a control system developed by Smith and Monroe (2021) to mitigate this imbalance, fairly rapid capacity fade and cell failure was repeatedly observed. The first 27 cycles of data in Fig. 1(a) show efficiency variations typical of these experiments. Similar trends have also been observed elsewhere (Clegg and Hill, 2020).

Smith posited that pore clogging in the separator was the primary driver of performance fade (Smith, 2021). As the pores within the membrane start to clog, the apparent coulombic efficiency of the cell rises, because smaller pores slow crossover of the active species. Once the membrane's pores drop below a critical size, exchange of the supporting electrolyte begins to be slowed, causing an apparent rise in membrane resistance and concomitant growth of charging and discharging overpotentials as shown in Fig. 1(b). These effects rationalize the monotonic rise in CE and decrease in VE that begins after cycle 6 and continues until cycle 27.

The data shown in Fig. 1 were produced by a cell in which the polarity was switched at cycle 28, i.e., the identities of the electrolyte reservoirs were swapped by running two discharge steps in a row at the end of cycle 27. This polarity reversal did not significantly impact the rate of voltage-efficiency change, indicating that the source of performance loss in the first 34 cycles was not a unidirectional (diode-like) phenomenon. The coulombic efficiency decreased by 5% immediately after the polarity switch but recovered after a single cycle. This likely owes to a transient effect associated with the development of diffusion layers with opposed gradients in the separator. Periodically steady concentration profiles of positively and negatively charged active species develop within the separator during cycling prior to the

polarity reversal; these act to neutralize the oppositely charged counterparts being forced into the membrane immediately after reversal, but the dramatic effect on CE vanishes after the diffusion layers re-establish with opposed gradients. Note that the decreasing UE during cycles 27–34 owes to the cell reaching its 3 V voltage cut-off before the targeted charge input.

The trend in voltage efficiencies in this experiment indicate that membrane fouling occurs within the membrane matrix, rather than on one of its faces, and is not reversible. This is further supported by the similarity of SEM images of the pristine and spent membrane (Fig. S2). At first glance the decrease in CE in Fig. 1(a) after the polarity switch might suggest reversible membrane fouling. However, Fig. 1(b, c) show that the charging and discharging overpotentials monotonically increase from cycles 1 to 35. Notably, once the polarity is reversed at cycle 28, the discharging overpotential jumps from 0.15 V to 0.3 V. This suggests that fouling within the membrane matrix is not symmetric and biased towards the positive side.

Upon cell failure (cycle 34, at which UE had dropped to nearly 0%), the porous separator and its flanking ePTFE gaskets were replaced, while all other cell components were retained. As can be seen in Fig. 1(a), cell performance was fully restored. Moreover, during cycles 35–60, the dynamical changes of CE and VE seen in cycles 1–34 essentially repeated, stemming from similar galvanostatic charge/discharge data (Fig. S3). Note that the ~5% decrease in UE after separator replacement owes to electrolyte loss during reassembly of the cell.

Cyclic voltammetry was performed on fresh and post-cycled V(acac)<sub>3</sub> electrolytes (Fig. S4), which both yielded similar voltammograms. These results support Smith's membrane fouling hypothesis, while contrasting other studies that point to degradation processes occurring at the negative electrode as the predominant cause of cell failure (Clegg and Hill, 2020).

#### 3.2. Canary cell experiments

After the microporous separator was identified as a main source of performance fade, a 3-cell experiment, in which two 'canary cells' were placed in series with the reactor being cycled, was conducted to probe whether performance of the Celgard 4560 separator changed during contact with charged electrolytes at open circuit. As shown in Fig. 2(a), both the positive and negative electrolytes were first passed in loops through canary cells at open circuit before flowing into the 'working cell', through which current was passed. No current was passed through the two canary cells, excepting the periods during which impedance spectra were gathered from them.

The cycling data and efficiencies from the working cell (Fig. S5) followed the same trends discussed above. Fig. 2(b-d) show stark differences between the impedance spectra of the canary cells and the working cell. The working cell's bulk area-specific resistance (ASR) –

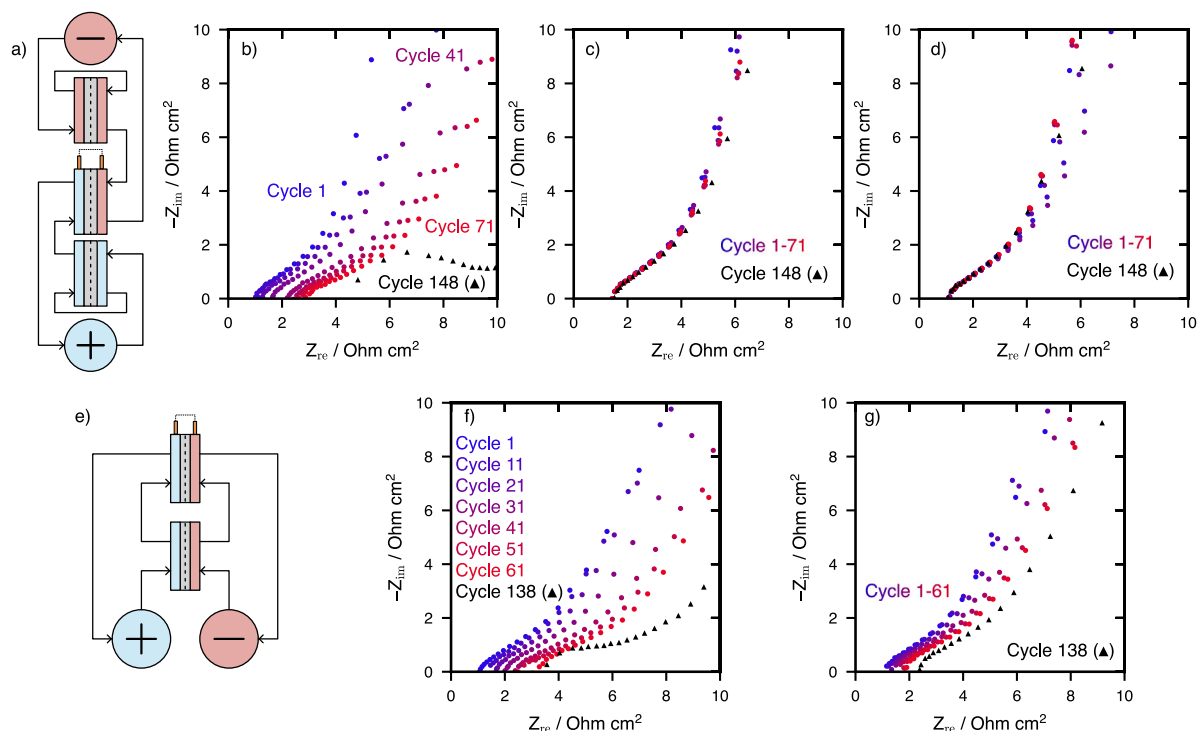


**Fig. 2.** Electrolyte flow configuration and Nyquist plots for the (a–d) 3-cell and (e–g) 2-cell canary experiments. An impedance measurement was taken for the (b, f) working and (c, d, g) canary cells every 10 cycles at 0% SOC (corresponding to a hold at 0 A applied current after discharge to 1.3 V). The signal amplitude was set to 10 mV and frequencies ranged from 0.1 Hz to 100 kHz with 5 points per decade.

as determined by the high frequency real intercept – increases from  $1.1 \Omega \text{ cm}^2$  to  $4.0 \Omega \text{ cm}^2$  over 148 cycles. This is naturally explained by gradual pore clogging in the separator: a smaller average pore size decreases the effective conductivity, increasing the cell's bulk resistance. In contrast, the bulk ASRs in both canary cells remained constant. Note that the positive cell's ASR is  $0.3 \Omega \text{ cm}^2$  larger than the negative's, owing to different resistances of the electrical leads, carbon-wool packing, etc.

The low-frequency responses of the canary cells vary due to slight differences in the SOC. Recall that impedance measurements were taken at 0% SOC as determined by holding at open circuit after the low-voltage cutoff was exceeded. Below 1.3 V, the slope of the open-circuit potential curve varies strongly with SOC. Because this effect manifests as an apparent zero-frequency admittance (inverse capacitance), small variations in the SOC near the cutoff voltage strongly impact the cell's low-frequency impedance response. Variations in the low-frequency imaginary impedance components of both canary cells were essentially random across cycles, but the variance was higher in the negative canary cell.

Excluding the differences in the low-frequency regime, the relatively constant impedance responses of both canary cells at moderate-to-high frequencies confirm that the Celgard 4560 separator performance remains stable in contact with charged electrolytes of either sign. Indeed, both canary cells were cycled after being disconnected from the 3-cell experiment and proceeded to indicate the pore clogging signature seen in the working cell: VE decreased monotonically and CE rose sigmoidally (Fig. S6). This observation is consistent with a hypothesis that pore clogging results from polarization of the cell—either a potential gradient associated with applied current or a concentration gradient associated with differences in charge state between solutions on either side of the membrane.

A 2-cell canary experiment was designed to probe the distinct effects of concentration and potential differences on membrane performance. In this configuration, shown in Fig. 2(e), the negative and positive electrolytes were passed through a canary cell before entering the working cell to experience applied current.

Similar to the 3-cell canary experiment, no current was passed through the concentration-polarized canary cell except during the periodic impedance measurements. This 2-cell experiment investigates a situation in which the working cell experiences forces that drive both diffusion and migration of electrolyte constituents across the membrane, whereas the canary cell only experiences a diffusion driving force. Nyquist plots for the working and canary cell are presented in Fig. 2(f, g). The bulk ASR increases in both cells as they cycle, but does so more slowly in the concentration-polarized canary cell. Over 138 cycles, the working cell's ASR increased by 220%, while the canary cell's rose by 120%. The combination of canary cell experiments suggests that no single species (charged or neutral) is solely responsible for membrane fouling; rather, the history of driving forces for migration and diffusion appears to propel the rise in separator resistance.

### 3.3. Evolution of crossover rates

Self-discharge tests were performed using the protocols described in Section 2.3 with Daramic 175 and Celgard 4560 microporous separators and at three different electrolyte flow rates. Fig. 3 presents representative data from the cell with a Daramic 175 separator and a  $51 \text{ mL min}^{-1}$  ( $5.0 \text{ cm s}^{-1}$ ) electrolyte flow rate. After every 10th cycle of charge–discharge, an impedance measurement was taken, after which the cell was charged via coulomb counting to 100% of the theoretical maximum SOC (assuming no crossover) and self-discharge was tracked. The charge–discharge data shown in Fig. 3(a) are similar to those seen in Section 3.1, but the charging and discharging overpotentials increase sharply after the self-discharge cycles, presumably because of the larger swings in SOC before them. Fig. 3(b) shows that the time to discharge to 2 V increases for each self-discharge cycle, consistent with the increasing coulombic efficiency trend seen in Fig. 1.

Impedance data were fitted to the equivalent circuit model depicted in Fig. 3(c). The cell resistance ( $R_\Omega$ ) is in series with both the negative ( $R_{\text{ct},1}$ ) and positive ( $R_{\text{ct},2}$ ) charge-transfer resistances and double-layer capacitances ( $C_{\text{dl},1}$  and  $C_{\text{dl},2}$ ). A finite-length Warburg element ( $W_s$ ) was

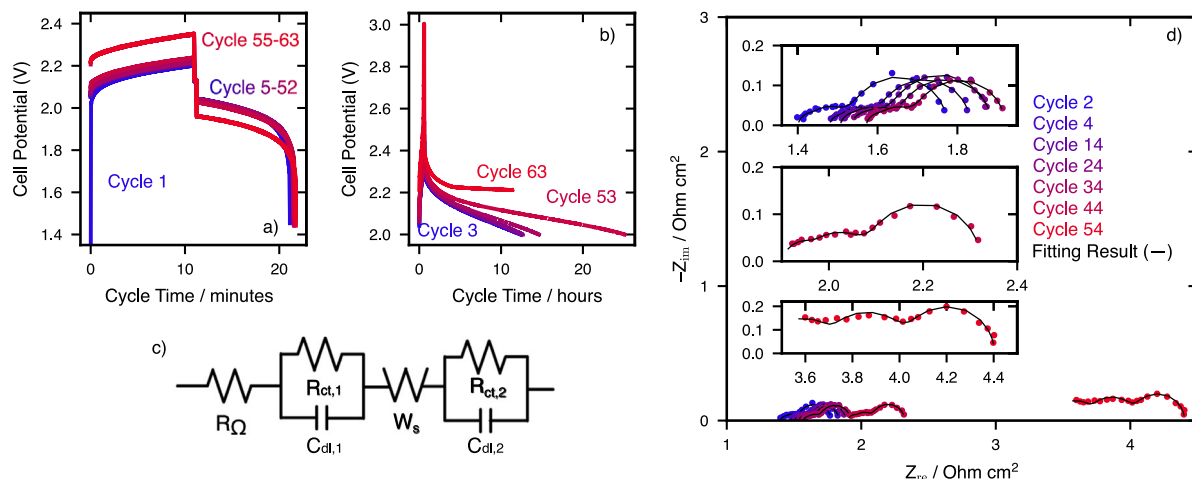


**Fig. 3.** (a) Charge-discharge curves for the 0.1 M V(acac)<sub>3</sub>/0.3 M TEABF<sub>4</sub>/ACN RFB chemistry with a Daramic 175 porous separator, a current density of 20 mA cm<sup>-2</sup>, and a mean linear flow velocity of 5.0 cm s<sup>-1</sup>. (b) Self-discharge curves (responses during a hold at 0 A applied current while relaxing to 2.0 V), which were measured every tenth cycle after cycle 3. (c) Equivalent circuit model used to fit (d) impedance data collected the cycle after each self-discharge step.

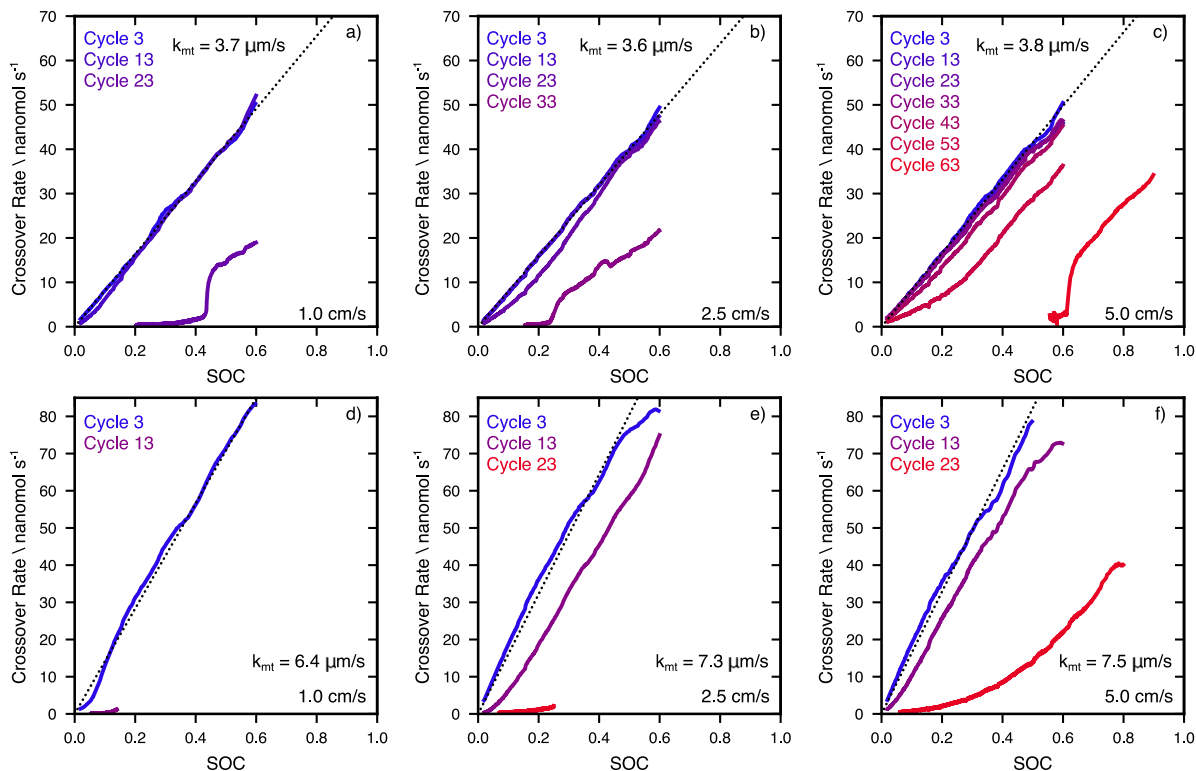


**Fig. 4.** Crossover estimation during each self-discharge cycle for the Daramic 175 (a–c) and Celgard 4560 (d–f) separators. Three mean linear flow rates, 1.0 cm s<sup>-1</sup> (a, d), 2.5 cm s<sup>-1</sup> (b, e), and 5.0 cm s<sup>-1</sup> (c, f), were tested. An adaptive observer was used to estimate all crossover rates from the voltage response (Ascencio et al., 2019). Mass transfer coefficients  $k_{mt}$  were calculated by linear fits (forced through zero) of the crossover estimates from the first self-discharge curve (cycle 3), in conjunction with the exposed membrane area  $A_x$  of 2.20 cm<sup>2</sup>. The coefficient of determination ( $R^2$  value) was greater than 0.99 in all instances.

added between the two interfacial reaction impedances to account for diffusion across the membrane. The fitted parameter that changed most was cell resistance: cycle 2 yielded a bulk ASR of 1.40 Ω cm<sup>2</sup>, which rose to 3.44 Ω cm<sup>2</sup> by cycle 54. The full list of fitted parameters is presented in Table S6. Similar trends were seen across all three flow rates and with both separators.

An adaptive observer governed by an isothermal, zero-dimensional ('stirred-tank') lumped-parameter model was reported earlier by Ascencio et al. (2019). The adaptive observer was used to estimate crossover rates dynamically during each self-discharge cycle. Notably, Ascencio's model does not assume that species fluxes through the

separator are proportional to the concentration difference across it (Fickian diffusion). Rather, the SOC and crossover flux are estimated simultaneously, allowing for signatures of more complex transport behavior to be extracted from the experimental voltage data.

Generally, the molar crossover flux  $Q_x$  of a charged species across a planar membrane normal to the  $x$  direction is expected to scale with both the exposed membrane area  $A_x$  and the concentration of the charged species. To first order, the relationship among these quantities can be parametrized by a mass-transfer coefficient  $k_{mt}$  with units of velocity, as

$$Q_x = k_{mt} A_x c_0 \text{SOC}_{\text{cell}}, \quad (4)$$



where  $c_0$  is the active-species concentration in the fully discharged electrolyte and  $\text{SOC}_{\text{cell}}$  is the SOC in the cell, which generally exceeds the reservoir SOC because the electrolytes accumulate excess charge during their residence time in the reactor chamber. For simple Fickian diffusion across the membrane,  $k_{\text{mt}}$  is expected to be a constant, proportional to the effective diffusivity of active species and inversely proportional to the membrane thickness. When diffusion is Fickian, the active observer is expected to show that  $Q_x$  varies in direct proportion to  $\text{SOC}_{\text{cell}}$ .

Fig. 4 shows crossover-rate estimates from the adaptive observer for both separators at three different mean linear velocities of  $1.0 \text{ cm s}^{-1}$ ,  $2.5 \text{ cm s}^{-1}$  and  $5.0 \text{ cm s}^{-1}$ . At the onset of cycling, the crossover is Fickian across both separators in all cases. These initial data sets were used to estimate  $k_{\text{mt}}$  values by linear regression; the dashed lines present the best-fit curves, and corresponding  $k_{\text{mt}}$  values derived from their slopes are written on the graphs in Fig. 4.

With the possible exception of Celgard at a  $1.0 \text{ cm s}^{-1}$  flowrate,  $k_{\text{mt}}$  for a particular membrane does not vary significantly with linear flowrate, suggesting that the flow in the reactor chamber was well-developed and turbulent. Linear regression shows that Daramic and Celgard have mass transfer coefficients of  $3.7 \mu\text{m s}^{-1}$  and  $6.4 \mu\text{m s}^{-1}$ , respectively, with a  $1.0 \text{ cm s}^{-1}$  linear flowrate through the reactor. The higher mass transfer coefficients seen for Celgard are consistent with the lower coulombic efficiencies they exhibit compared to the Daramic separator (Yuan et al., 2021).

The  $k_{\text{mt}}$  value remains essentially unchanged for Daramic as flowrate rises, signifying that convection has little impact on the initial crossover rate of active species. For Celgard, the mass transfer does increase by about 15% as the flowrate increases from  $1.0 \text{ cm s}^{-1}$  to  $4.9 \text{ cm s}^{-1}$ . It appears that most of this increase occurs between the flowrates of  $1.0 \text{ cm s}^{-1}$  and  $2.5 \text{ cm s}^{-1}$ . Possibly there is a critical flow rate at which the flow becomes well-developed and turbulent within the reactor chamber, such that  $k_{\text{mt}}$  ceases to change. Given the electrolyte's viscosity of  $0.535 \text{ cP}$  (Saraidaridis and Monroe, 2019) and reactor dimensions, turbulent mixing ( $\text{Re} > 4000$ ) would occur at a linear flow rate of  $16 \text{ cm s}^{-1}$ —within an order of magnitude of the tested flow rates. The experimentally reported linearized velocities do not account for the tortuosity and compression of the porous electrode, suggesting that their true values are larger than reported. Note that a similar trend was seen for the Daramic separator at flow rates below  $1.0 \text{ cm s}^{-1}$  but the long residence times at these low rates led to very high per-pass conversion, and consequently large overpotentials, that caused the voltage cutoffs to be reached before significant amounts of charge could be exchanged at the current density used for these experiments.

As cycling progresses for each cell, the adaptive observer shows that the law governing crossover deviates from the expected Fickian response. For example, the Daramic cell run at a linear flow rate of  $5.0 \text{ cm s}^{-1}$ , shown in Fig. 4(c), maintains a constant, Fickian mass transfer coefficient for the first 33 cycles. During cycles 43 and 53, the crossover rate begins to be suppressed at low SOC; after reaching SOC greater than 40%, however, the slope of the crossover vs. SOC curve reaches a value commensurate with the  $k_{\text{mt}}$  observed in earlier cycles. By cycle 63, the crossover rate suddenly drops to roughly zero below 60% SOC. Similar trends are seen for the  $1.0 \text{ cm s}^{-1}$  and  $2.5 \text{ cm s}^{-1}$  flow rates, although the cells survive for fewer cycles.

Remembering that SOC is a proxy for the concentration polarization across the membrane, and consequently with the thermodynamic force that drives diffusion, the trends exhibited in Fig. 4 are commensurate with pore clogging. We hypothesize that in Daramic, the average pore size establishes a minimum threshold for the diffusion driving force needed to drive supporting-ion exchange across the membrane. As cycling proceeds, the average pore size in the membrane shrinks, and this critical diffusion driving force rises. Falling crossover rates are observed in Celgard as well, but the variation in crossover rate with SOC is more indicative of a gradual change in effective diffusivity with SOC,

rather than a sudden transition from blocking to Fickian behavior at a threshold SOC. The qualitatively distinct fouling signatures between Daramic and Celgard have been hypothesized to stem from differences in their mechanical properties and microstructure, outlined in Table S8 (MacHado et al., 2021).

#### 4. Conclusions

Although side reactions have been proposed as the predominant degradation pathway for the  $\text{V}(\text{acac})_3/\text{TEABF}_4/\text{ACN}$  RFB chemistry, we observed that membrane fouling was the primary driver of cell failure. The widely reported increase in coulombic efficiency and steady drop in voltage efficiency over the first few dozen cycles relates to changes in the membrane separator, rather than deterioration of the active electrolytes. After replacement of the Celgard membrane, the initial capacity and efficiency metrics of a flow reactor were recovered entirely.

If the membrane-fouling problem can be solved, porous separators with appropriate modifications may allow coulombic efficiencies comparable to those achieved with more costly bespoke ion-exchange membranes. Canary cells showed that Celgard 4560 is stable and maintains a constant resistance when exposed to both positively and negatively charged electrolyte solutions. The resistivity increased when exposed to current and, less significantly, when exposed to an electrolyte composition difference. Our observations suggest that the resistance rises can be explained by pore clogging, although the signature of this effect differs between Daramic and Celgard.

In the initial cycles, the crossover rates across both Celgard and Daramic porous separators were directly proportional to SOC, consistent with a Fickian diffusion process. Mass-transfer coefficients did not vary significantly with electrolyte flowrate and were  $3.8$  and  $7.5 \mu\text{m s}^{-1}$  at mean linear flowrates of  $5.0 \text{ cm s}^{-1}$  for Daramic 175 and Celgard 4560, respectively. Crossover rates deviated from Fickian responses as membrane fouling progressed. The crossover rate dropped suddenly at a rising threshold SOC for Daramic 175, whereas it gradually dropped with respect to SOC for Celgard 4560, suggesting that the two membranes foul by disparate mechanisms.

#### CRedit authorship contribution statement

**Rohit Rungta:** Writing – original draft, Software, Methodology, Investigation, Formal analysis, Data curation, Conceptualization. **Kirk P. Smith:** Methodology, Conceptualization. **Charles W. Monroe:** Writing – review & editing, Supervision, Methodology, Formal analysis, Conceptualization.

#### Declaration of competing interest

The authors declare the following financial interests/personal relationships which may be considered as potential competing interests: Charles W. Monroe reports financial support was provided by The Faraday Institution. Kirk P. Smith reports financial support was provided by The Faraday Institution. If there are other authors, they declare that they have no known competing financial interests or personal relationships that could have appeared to influence the work reported in this paper.

#### Data availability

Data will be made available on request.

#### Acknowledgments

This work was supported in part by the Faraday Institution Multiscale Modelling project, subaward FIRG059 under Grant EP/S003 053/1. R.R. was supported by the DW Morphy Graduate Scholarship.

## Appendix A. Supplementary data

Supplementary material related to this article can be found online at <https://doi.org/10.1016/j.memlet.2024.100074>. This file contains reactor schematics, SEM images of membranes before and after cycling, and more electrochemical data.

## References

- Ascencio, P., Smith, K., Monroe, C., Howey, D., 2019. Adaptive observer for charge-state and crossover estimation in disproportionation redox flow batteries undergoing self-discharge. In: 2019 American Control Conference. <http://dx.doi.org/10.23919/ACC.2019.8814764>.
- Carley, S., Davies, L.L., Spence, D.B., Zirogiannis, N., 2018. Empirical evaluation of the stringency and design of renewable portfolio standards. *Nature Energy* 3, 754–763. <http://dx.doi.org/10.1038/s41560-018-0202-4>.
- Clegg, C., Hill, I.G., 2020. Characterizing degradation in non-aqueous vanadium(III) acetylacetonate redox flow batteries. *J. Electrochem. Soc.* 167, 120510. <http://dx.doi.org/10.1149/1945-7111/aba932>.
- Darling, R.M., Gallagher, K.G., Kowalski, J.A., Ha, S., Brushett, F.R., 2014. Pathways to low-cost electrochemical energy storage: A comparison of aqueous and nonaqueous flow batteries. *Energy Environ. Sci.* 7, 3459–3477. <http://dx.doi.org/10.1039/c4ee02158d>.
- Escalante-García, I.L., Wainright, J.S., Thompson, L.T., Savinell, R.F., 2015. Performance of a non-aqueous vanadium acetylacetonate prototype redox flow battery: Examination of separators and capacity decay. *J. Electrochem. Soc.* 162, A363–A372. <http://dx.doi.org/10.1149/2.0471503jes>.
- Judson, J., Pike, S., 2015. State of charge: A comprehensive study of energy storage in Massachusetts. Massachusetts Energy Storage Initiative. <https://www.mass.gov/media/6436/download>.
- Lehmann, M.L., Tyler, L., Self, E.C., Yang, G., Nanda, J., Saito, T., 2022. Membrane design for non-aqueous redox flow batteries: Current status and path forward. *Chem* 8, 1611–1636. <http://dx.doi.org/10.1016/j.chempr.2022.04.005>.
- Liu, Q., Sleightholme, A.E., Shinkle, A.A., Li, Y., Thompson, L.T., 2009. Non-aqueous vanadium acetylacetonate electrolyte for redox flow batteries. *Electrochem. Commun.* 11, 2312–2315. <http://dx.doi.org/10.1016/j.elecom.2009.10.006>.
- Luo, W., Stynski, S., Chub, A., Franquelo, L.G., Malinowski, M., Vinnikov, D., 2021. Utility-scale energy storage systems: A comprehensive review of their applications, challenges, and future directions. *IEEE Ind. Electron. Mag.* 15, 17–27. <http://dx.doi.org/10.1109/MIE.2020.3026169>.
- MacHado, C.A., Brown, G.O., Yang, R., Hopkins, T.E., Pribyl, J.G., Epps, T.H., 2021. Redox flow battery membranes: Improving battery performance by leveraging structure–property relationships. *ACS Energy Lett.* 6, 158–176. <http://dx.doi.org/10.1021/acsenergylett.0c02205>.
- Palmer, G., 2019. Renewables rise above fossil fuels. *Nature Energy* 4, 538–539. <http://dx.doi.org/10.1038/s41560-019-0426-y>.
- Rungta, R., 2023. Data and code for drivers of membrane fouling in the vanadium acetylacetonate flow battery. <http://dx.doi.org/10.5287/ora-rbe2g7ebb>, URL <https://ora.ox.ac.uk/objects/uuid:d56ac0e3-c629-4ae3-a5a9-9d220efbedc1>.
- Saraidaridis, J.D., Monroe, C.W., 2019. Nonaqueous vanadium disproportionation flow batteries with porous separators cycle stably and tolerate high current density. *J. Power Sources* 412, 384–390. <http://dx.doi.org/10.1016/j.jpowsour.2018.11.058>.
- Shinkle, A.A., Sleightholme, A.E., Griffith, L.D., Thompson, L.T., Monroe, C.W., 2012. Degradation mechanisms in the non-aqueous vanadium acetylacetonate redox flow battery. *J. Power Sources* 206, 490–496. <http://dx.doi.org/10.1016/j.jpowsour.2010.12.096>.
- Shinkle, A.A., Sleightholme, A.E., Thompson, L.T., Monroe, C.W., 2011. Electrode kinetics in non-aqueous vanadium acetylacetonate redox flow batteries. *J. Appl. Electrochem.* 41, 1191–1199. <http://dx.doi.org/10.1007/s10800-011-0314-z>.
- Smith, K., 2021. Symmetric nonaqueous flow batteries with porous separators. Doctoral dissertation, University of Oxford. <https://ora.ox.ac.uk/objects/uuid:23eec36c-3ec7-4ae9-9ab8-526681121466>.
- Smith, K.P., Monroe, C.W., 2021. Image-based mechanical balancing of reservoir volumes during benchtop flow battery operation. *Front. Chem. Eng.* 3, <http://dx.doi.org/10.3389/fceng.2021.748865>.
- Weber, A.Z., Mench, M.M., Meyers, J.P., Ross, P.N., Gostick, J.T., Liu, Q., 2011. Redox flow batteries: A review. *J. Appl. Electrochem.* 41, 1137–1164. <http://dx.doi.org/10.1007/s10800-011-0348-2>.
- Yuan, J., Pan, Z.Z., Jin, Y., Qiu, Q., Zhang, C., Zhao, Y., Li, Y., 2021. Membranes in non-aqueous redox flow battery: A review. <http://dx.doi.org/10.1016/j.jpowsour.2021.229983>.